

Article

On the Flow of CO₂-Saturated Water in a Cement Fracture

De Nyago Tafen^{1,2,*}, Barbara Kutchko³ and Mehrdad Massoudi^{3,*} 

¹ U.S. Department of Energy, National Energy Technology Laboratory, 1450 Queen Avenue SW, Albany, OR 97321, USA

² NETL Support Contractor, 1450 Queen Avenue SW, Albany, OR 97321, USA

³ U.S. Department of Energy, National Energy Technology Laboratory, 626 Cochran Mill Road, Pittsburgh, PA 15236, USA; barbara.kutchko@netl.doe.gov

* Correspondence: denyago.tafen@netl.doe.gov (D.N.T.); mehrdad.massoudi@netl.doe.gov (M.M.)

Abstract: Cement fractures represent preferential leakage pathways in abandoned wells upon exposure to a CO₂-rich fluid. Understanding fracture alteration resulting from geochemical reactions is critical for assessing well integrity in CO₂ storage. This paper describes a mathematical model used to investigate the physical and the chemical changes in cement properties when CO₂-saturated water is injected into a wellbore. This study examines the flow of a solution of CO₂-saturated water in a two-dimensional fractured cement. In this approach, a micro-continuum equation based on the Darcy–Brinkman–Stokes (DBS) equation is used as the momentum balance equation; in addition, reactive transport equations are used to study the coupled processes of reactant transport and geochemical reactions, and the model for cement porosity alteration and fracture enhancement. This paper focuses on the effects of cement porosity, fracture aperture size, and surface roughness. Mineral dissolution and precipitation mechanisms are also considered. Our simulations show that smaller initial fracture apertures tend to a high mineral precipitation self-sealing. However, a complete sealing of the fracture is not observed due to the continuous flow of CO₂-saturated water. The calcite precipitation mechanism of a rough fracture (random zigzag shape) differs from that of a smooth/flat fracture surface.

Keywords: reactive transport in fracture; multiscale simulations; micro-continuum; porousMedia4Foam; mineral dissolution; cement



Citation: Tafen, D.N.; Kutchko, B.; Massoudi, M. On the Flow of CO₂-Saturated Water in a Cement Fracture. *Geosciences* **2023**, *13*, 312. <https://doi.org/10.3390/geosciences13100312>

Academic Editors: Martin Ma, Xiao Tian, Meng Lu and Jesus Martinez-Frias

Received: 9 August 2023
Revised: 29 September 2023
Accepted: 16 October 2023
Published: 17 October 2023



Copyright: © 2023 by the authors. Licensee MDPI, Basel, Switzerland. This article is an open access article distributed under the terms and conditions of the Creative Commons Attribution (CC BY) license (<https://creativecommons.org/licenses/by/4.0/>).

1. Introduction

Studies have shown that carbon capture and storage (CCS) can significantly help to reduce greenhouse gas emissions [1]. In many geoscience applications, CO₂ is captured and injected into geological formations for permanent storage [2]. For this to happen, the CO₂ needs to be transported to the proper location, and, in some cases, expansion valves are used to release supercritical CO₂ from high-pressure containers to the selected injection site. Due to the Joule–Thomson cooling effect, the reduction in the temperature of the released CO₂ stream might induce the thermal contraction of the injection well causing fracture instability in the storage formation [3]. The Joule–Thomson effect may cause pressure fluctuation, which can cause fracture.

A recent study by Khan et al. [4] indicates that using saturated water or brine with CO₂ at the surface prior to injection can change “the dominant trapping mechanism from ‘structural’ and ‘residual’ to more stable ‘solution trapping’”. Importantly, the saturated brine is often slightly denser than the virgin reservoir fluid”. The risk of the migration or leakage of the buoyant CO₂ stream through the seal or fractures is a major challenge in carbon storage. As mentioned by Le Gallo and De Dios, the storage reservoir is sometimes in a deep saline aquifer with natural fractured carbonates, and understanding or predicting CO₂ migration in these formations is important for the safety of the operation [5]. Interestingly, as Phuoc et al. indicate, when a fluid flows upward in such an arrangement in a well

or a fracture, its temperature and pressure, in general, decrease [6]. The decrease in the pressure can be attributed to the gravitational and the frictional effects, and the reduction in the temperature can be due the gravitational effect, frictional effect, the Joule–Thomson cooling/heating effect, and the heat loss via heat conduction to the surrounding rock formation. This heat loss can cause thermally induced stresses large enough to cause a significant contribution to the existing earth stresses, which can potentially fracture the rock [7].

One of the threats of carbon capture and its storage is the potential leakage of CO₂ from storage reservoirs due to the tendency of the injected fluid to migrate upward mainly due to buoyancy. Active and abandoned wells often present geological formations such as existing interfaces, faults, and fractures, which can become pathways for potential leakage. Often, these preferential pathways occur on the wellbore cement used to seal the reservoirs arising from chemical reactions or mechanical failures. Therefore, understanding the dynamic evolution of these preferential pathways is critical for the integrity of well cement. In general, understanding the transient multiphase flow of CO₂-saturated water in a wellbore is crucial not only for the design of wells but also for assessing the operational risk [8]. To understand and mitigate a potential leakage of CO₂ from geological carbon storage systems, numerical modeling and experimental studies have been conducted in recent years to investigate the flow of CO₂-saturated fluid through fractured cement [9–13].

Three different kinds of models have been developed to describe the flow and the reactive transport in fractured cement. The continuum-scale model, which is the most common approach, uses a porosity–permeability relationship, in the form of Darcy’s equation, and an effective diffusion coefficient and surface area to characterize the flow and the geochemical reactions. For example, Cao et al. used a continuum model to study the self-healing of cement fractures under the dynamic flow of a CO₂-rich brine by carrying out a reactive flow-through experiment and developed a simplified 2-D reactive transport model with parameters derived from experiments [9]. The model used a uniform fracture plane, where the flow field was represented by Darcy’s equation. The fracture properties and the conditions where fracture opening and fracture clogging occur were examined by varying the aperture size, flow rate, and fracture length. Their results showed that the residence time and the size of the initial fracture aperture are among the key parameters controlling the self-healing or fracture opening behavior. They observed that a longer residence time and small apertures promote mineral precipitation, fracture closure, and therefore flow restriction.

Brunet et al. developed a process-based model to investigate the reactive transport characteristics and the key parameters that control the self-sealing and the fracture opening behavior of cement fractures exposed to carbonated water under conditions relevant to geological carbon sequestration [12]. The model was used to predict the long-term effects of carbonated brine leakage on the fractured cement cores by varying the initial aperture size, the pressure gradient (initial flow rate), and the cement core length. However, Darcy-scale models of fractured domains tend to oversimplify the flow within the fracture, and, therefore, these models cannot capture the transport limitation in the fracture toward its surfaces [14,15].

Recent advances in microscopic characterizations and computational capabilities have seen the emergence of pore-scale models, where the pore network is fully resolved, and the physics is better understood, with the interest of upscaling the results to a macroscopic Darcy-like representation [16–23]. One of the major challenges of this approach is the modeling of dissolution/precipitation problems, which is made difficult because of the moving fluid/solid boundary with respect to the chemical reactions occurring at the mineral boundaries [24].

Porous geological formations occurring in nature often have complex multiscale features, resulting in scale-dependent properties, which limits the use of pure pore-scale models. To account for coupled processes and parameters, hybrid-scale models have been developed to describe systems that span multiple characteristic length scales. In that regard,

flow and reactive transport in fractured cement can be regarded as a multiscale problem that couples a pore-scale component in the fracture and a continuum-scale component in the cement matrix [25,26]. Hybrid-scale models can be solved using the domain decomposition technique, where the flows in the fracture and the cement matrix are governed by two different equations, coupled together through appropriate boundary conditions, for example, enforcing mass and momentum continuity at the interface [25,27].

Another implementation of a hybrid-scale model uses a single set of partial differential equations, the Darcy–Brinkman–Stokes (DBS) equation, in a single micro-continuum domain [28–30]. In the pore space (fracture), terms associated with the porous media flow become negligible, and in the porous continuum (cement matrix), the terms associated with the pore-scale become negligible. Although the micro-continuum approach presents several advantages in capturing the reactive transport processes through the porous and the solid-free regions, it has been applied to only a very few studies to simulate reactive transport in fractured media. For example, You and Lee employed the Darcy–Brinkmann–Stokes pore-scale approach to investigate the effects of fracture surface roughness on the acid reactive transport and the dissolution mechanisms of porous media with natural fractures [31]. The porous media considered consisted of a single mineral, calcite. In our calculations, fractured cement is composed of multiple minerals inert with each other. Zhang et al. used a micro-continuum approach to study the reactive transport processes in fractured media with emphasis on the porous altered layer bordering the fracture and their impacts on fracture alteration [32]. Their simulations included the advection, diffusion, and dissolution of both fast- and slow-reacting minerals.

Experimentally, Min et al. investigated the alteration of fractured foamed cement exposed to CO₂-saturated water [33]. Foam quality was varied to determine the impact of the CO₂-saturated water flowing along a fracture in the cement. Foamed cements with 20 and 30% of air volumes were used. The study was performed to understand the difference in the sealing behavior of foamed cement and conventional cement, the impact of bubbles on fracture roughness or aperture, the impact of fluid flow on fracture, opening vs. clogging, and the impact of foam quality on the fracture mechanical properties. In the experimental setup, the cement cores were of a cylindrical shape of diameter 2.54 cm with lengths between 3.5 and 12.5 cm, and the fracture of the initial aperture was less than 1 mm. The cement cores were placed horizontally, and a solution of CO₂-saturated water was injected into the fracture at a constant rate and room temperature. The self-sealing of the fractures in the cement was observed at a flow rate of 0.1 mL/min and a pressure of 6.9 MPa. The authors concluded that self-sealing was likely due to the formation of CaCO₃ precipitations.

The objective of this work is to investigate the impact of CO₂-saturated water flowing along a fracture in cement using a micro-continuum approach. For a recent review of the many existing approaches to the formulation and simulation of CO₂ flow in fractures, we refer to the review report by Tafen et al. [34]. We focus on the effects of cement porosity, fracture aperture size, and surface roughness. Mineral dissolution and precipitation reactions are assumed to take place in the cement. The difference from previous models (for example, Brunet et al. [12]) is that we use a hybrid-scale model instead of a continuum-scale approach to model the flow and the transport in the system, and we also consider surface roughness. The fractured cement is represented by a two-dimensional rectangular domain, with a fracture embedded in the rectangle (Figure 1). The cement matrix is modeled as a porous medium composed of minerals. In the hydrated class H cement, the major components are semi-amorphous calcium silicate hydrate gel (C–S–H) and crystalline portlandite (Ca(OH)₂). They occupy more than 70% of the total hydrated cement volume [35–37]. Therefore, the minerals that compose our porous medium can be limited to C-S-H and Ca(OH)₂. We use a micro-continuum approach, where the flow in the fracture is represented by the Navier–Stokes equations, and the cement matrix is modeled as a porous medium, where the flow is governed by Darcy’s equation. Throughout the manuscript, the fluid refers to CO₂-saturated water.

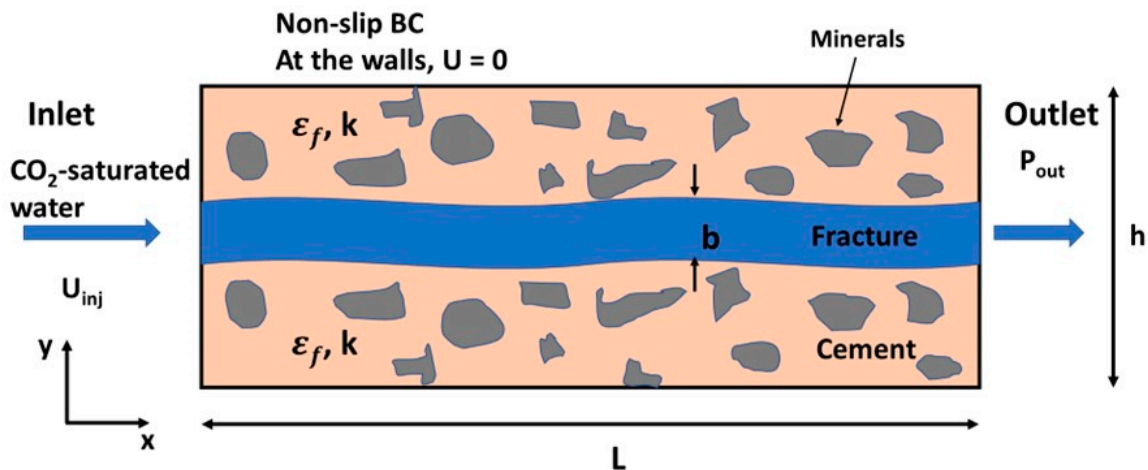


Figure 1. The physical setup of a fracture embedded in a reactive porous medium. The porous medium is a cement composed of minerals. The injection fluid is a solution of CO₂-saturated water. The fluid is injected from left to right.

2. Materials and Methods

This section provides the governing equations and the simulation setup.

2.1. Governing Equations

Rather than treating the fluid and the cement matrix as two separate subdomains, one can consider a single domain, where the fluid/solid interfaces are not explicitly resolved. In this approach, the flow is described by the Darcy–Brinkman–Stokes equation, also referred to as the micro-continuum approach by Soulaïne and Tchelepî [29].

The micro-continuum approach is based on the volume averaging of the governing equations over each control volume [38,39]. The fluid/solid interface is tracked in terms of the volume of fluid (which is also the pore or the void space that can be occupied by the fluid), V_f , and the solid phase, V_s , in each control volume V , and their volume fraction $\epsilon_f = V_f/V$ and $\epsilon_s = 1 - \epsilon_f$. For $\epsilon_f = 1$, we have only fluid, and, when $\epsilon_f = 0$, we have only solid (no pore space; hence, no fluid flow can take place). ϵ_f also defines the local porosity field of the medium. At the fluid/solid interface, $0 < \epsilon_f < 1$. In each control volume, all the physical variables are volume averages, and the flow in the fractured cement can be described using the single field balance of the momentum equation arising from the integration of the Navier–Stokes equation [40–45]:

$$\frac{1}{\epsilon_f} \left(\frac{\partial \rho_f \mathbf{u}}{\partial t} + \nabla \cdot \left(\frac{\rho_f}{\epsilon_f} \mathbf{u} \mathbf{u} \right) \right) = -\nabla p + \nabla \cdot \left(\frac{\mu_f}{\epsilon_f} (\nabla \mathbf{u} + \nabla \mathbf{u}^t) \right) - \mu_f k^{-1} \mathbf{u}, \tag{1}$$

where ρ_f and μ_f are the CO₂-saturated water density and viscosity, respectively, and k is the local or the cell permeability. The pressure field, p , and the velocity field, \mathbf{u} , are the unknowns of the system. The second term on the right-hand side represents the dissipative viscous forces, where $\nabla \mathbf{u}^t$ is the transpose of $\nabla \mathbf{u}$. The last term, the drag force or the Darcy resistance term ($\mu_f k^{-1} \mathbf{u}$), is due to the momentum exchange between the fluid and the cement [46]. This term is dominant in the cement matrix, where the permeability is low, and it vanishes in the fracture (solid-free zone), where the permeability is very large or infinite. We assume the local permeability field k to be a function of the local porosity ϵ_f based on the Kozeny–Carman relationship,

$$k = k_0 \left(\frac{\epsilon_f}{\epsilon_{f,0}} \right)^\alpha \left(\frac{1 - \epsilon_{f,0}}{1 - \epsilon_f} \right)^\beta, \tag{2}$$

where k_0 and $\varepsilon_{f,0}$ are the initial permeability and the porosity of the porous medium, respectively. We also assume that the CO₂-saturated water viscosity is constant. In general, μ_f can depend on time, temperature, pressure, and other quantities.

The mass conservation equation for the CO₂-saturated water can be written as

$$\frac{\partial \varepsilon_f \rho_f}{\partial t} + \nabla \cdot (\rho_f \mathbf{u}) = \dot{m}, \tag{3}$$

where \dot{m} is the mass transfer rate of the fluid/cement. If minerals from the cement are transferred into the fluid (e.g., during dissolution processes), this quantity is positive. It is negative during precipitation processes and equals 0 if no precipitation or dissolution occurs. Assuming that more than one type of mineral in the foamed cement is reacting, the evolution of the volume fraction of the cement in a control volume will be governed by the following mass balance equations [29]:

$$\frac{\partial \omega_{s,j} \rho_{s,j}}{\partial t} = -\dot{m}_{s,j} \quad \text{with } j = 1, \dots, N_s, \tag{4}$$

where $\rho_{s,j}$ is the density of mineral j , $\dot{m}_{s,j}$ is the mass exchange term of mineral j with the fluid, N_s is the total number of minerals in the foamed cement, and $\omega_{s,j}$ is the volume fraction of mineral j and obeys the following relation:

$$\varepsilon_s = \sum_{j=1}^{N_s} \omega_{s,j}. \tag{5}$$

The summation of Equation (4) over all the minerals in the cement matrix gives

$$\dot{m} = \sum_{j=1}^{N_s} \dot{m}_{s,j}. \tag{6}$$

The transport of CO₂-saturated water is described by the mass balance equation averaged over the control volume [45]:

$$\frac{\partial \varepsilon_f c_f}{\partial t} + \nabla \cdot (\mathbf{u} c_f) - \nabla \cdot (\varepsilon_f D_f^* \cdot \nabla c_f) = -R_f, \tag{7}$$

where D_f^* is an effective diffusion tensor of the fluid. The quantities c_f and R_f are the concentration of the CO₂-saturated water and the changes in the concentration of the CO₂-saturated water due to reactions with minerals, respectively. We assumed that the foamed cement is composed of N_s -reacting minerals; thus, $R_f = c_f \sum_j A_{s,j} r_j$, where $A_{s,j}$ is the reactive surface area of mineral j in the cement, and r_j is the constant of the reaction of the CO₂-saturated water with mineral j . For a given mineral, r_j can be obtained through the transition state theory rate law [47].

During the dissolution/precipitation process, the volume fraction of the minerals changes. The change in the volume fraction of the minerals in the cement evolves according to the following equation:

$$\frac{\partial \omega_{s,j}}{\partial t} = -A_{s,j} r_j V_{m,j} c_f, \tag{8}$$

where $V_{m,j}$ is the molar volume (molecular weight/density) of the reacting mineral j [48]. Making use of Equation (5), the porosity of the foamed cement evolves according to the following:

$$\varepsilon_f = 1 - \sum_{j=1}^{N_s} \omega_{s,j} \tag{9}$$

The permeability of the cement is updated at every time step according to Equation (2). The reactive surface areas $A_{s,j}$ of all minerals are updated according to a power law model

$$A_{s,j} = A_{0,j}(\omega_{s,j})^n, \quad (10)$$

where $A_{0,j}$ is the initial reactive surface area of the minerals, $\omega_{s,j}$ is the volume fraction of the minerals, and n is a user-defined exponent [49,50].

The fracture is differentiated from the porous medium by assigning different values to the porosity field, ε_f , and to the permeability, k . In Figure 1, the blue color corresponds to the fracture ($\varepsilon_f = 1$), where the flow is governed by the Stokes equations ($k^{-1} = 0 \text{ m}^{-2}$), and the peach color refers to the foamed cement matrix, which is modeled as a porous medium with porosity field $0 < \varepsilon_f < 1$ and initial permeability. A solution of the CO₂-saturated water is continuously injected through the inlet (left-hand side boundary) at a constant flow rate throughout the simulation period,

$$u|_{x=0} = U_{inj} \quad (11)$$

The top and bottom walls of the fractured cement are set as non-slip boundary conditions,

$$u|_{y=0, y=h} = 0 \quad (12)$$

At the inlet, the concentration of the CO₂-saturated water is assumed to be constant

$$c_f|_{x=0} = c_{f0} \quad (13)$$

Across the top and bottom boundary walls, the mass transfer is assumed to be zero. Therefore,

$$\frac{\partial c_f}{\partial n}|_{y=0, y=h} = 0 \quad (14)$$

At the outlet, we use a fixed pressure boundary condition, and no concentration gradients is allowed:

$$p|_{x=L} = P_{out} \quad (15)$$

$$\frac{\partial c_f}{\partial n}|_{x=L} = 0 \quad (16)$$

The effective diffusion tensor of the fluid in Equation (7), D_f^* , combines diffusion and dispersion and can be written as a sum of molecular diffusion D_f and hydrodynamic dispersion α_L according to the following expression [51] (pp. 579–663):

$$D_f^* = (\varepsilon_f)^\eta D_f \left(1 + \frac{\alpha_L}{D_f} |\mathbf{u}| \right), \quad (17)$$

where η is the cementation factor that accounts for the tortuosity of the cement matrix, D_f is the molecular diffusion coefficient of the CO₂ in the water, and α_L is the hydrodynamic dispersion coefficient. In our simulations, we assume that $\alpha_L = 0$ and $\eta = 1/3$. For a summary of the variables to be calculated, see Table 1.

Table 1. Summary of the unknown variables and the governing equations along with the initial and the boundary conditions.

Unknown Variables	Equation Numbers	Initial Conditions	Boundary Conditions
p, \mathbf{u}	(1)	U_{inj}	$\mathbf{u} = 0$ at walls $p _{x=L} = P_{out}$
c_f	(7)	$c_{f,0}$	$\frac{\partial c_f}{\partial n} = 0$
$\omega_{s,j}$	(8)	$\omega_{s,0j}$	

The reactive transport problem is solved using the open-source solver porousMedia4Foam developed by Soullaine et al. and implemented in the open-source computational fluid dynamics (CFD) platform OpenFoam (<https://www.openfoam.com>, accessed on 8 August 2023) [45]. The flow model is discretized using the finite-volume method and solved sequentially. The pressure–velocity coupling is handled using a predictor–corrector strategy based on the PIMPLE algorithm, which is a combination of PISO (Pressure Implicit with Splitting of Operator, Issa, 1985) and SIMPLE (Semi-Implicit Method for Pressure Linked Equations, Patankar, 1980), as implemented in OpenFoam [52,53]. The advection–diffusion–reaction equation for the transport of the CO₂-saturated water is discretized on the computational grid using the finite-volume method and solved implicitly. The geochemistry part of porousMedia4Foam is exclusively handled using PHREEQC to solve the geochemical interactions [54]. Essential information such as the concentration of the species and the minerals between the flow solver and the geochemical solver PHREEQC is transferred through the module PhreeqcRM [55]. The multiscale capabilities of porousMedia4Foam are demonstrated in References [45,56].

2.2. Numerical Setup

Simplified 2-D reactive transport is developed to represent the flow of CO₂-saturated water in a fractured cement (Figure 1). We use a domain size of 12 cm × 2.54 cm with an initial fracture aperture size of 12 μm. These parameters are chosen to be consistent with the available experiments [33]. The domain is discretized into (100 × 25) grid blocks. Smaller grids are used along the fracture width direction (perpendicular to the main flow direction) with a resolution of 2.4 μm. The physical and geochemical conditions of the experiment are used in the model, including the average fracture aperture size, CO₂-saturated water concentration and pH value, and flow conditions. For the simulations, we use a cement composition of 16% portlandite and 62% C-S-H in volume with an initial porosity of 22% based on previous work [12,57,58]. A solution of CO₂-saturated water at pH 3.0 is continuously injected from the inlet boundary at a constant rate of 0.1 mL/min. The initial conditions and a description of the primary components continuously injected into the system are provided in Table 2. The initial permeability of the cement is taken from Min et al. and is $k_0 = 9.4 \times 10^{-15} \text{ m}^2$ [33]. The reactive surface areas (A_0) of the C-S-H, portlandite, and calcite are taken from Davila et al. and are 20,000, 300, and $50 \text{ m}^2/\text{m}^3_{\text{mineral}}$ [59]. The rates of the reactions are calculated from the reaction network in Table 3, which includes both thermodynamic-controlled aqueous reactions and kinetic-controlled mineral dissolution and precipitation reactions. The diffusion coefficient of the CO₂-saturated water is taken to be $\sim 10^{-9} \text{ m}^2/\text{s}$, as in Brunet et al. [12], and it varies as a function of porosity according to Equation (17).

Table 2. Initial conditions and the description of the primary components injected in the fractured cement.

Primary Components	Units	Initial Condition	Injected Solution
pH	-	13	3
CO ₃ ²⁻	mol/kgw	1.5	1.5
Ca ²⁺	mol/kgw	0.001	10 ⁻²⁰
Si	mol/kgw	-	10 ⁻²⁰

Table 3. Chemical reactions of CO₂-cement interactions, reaction thermodynamics, and kinetics [60–62].

Reaction	log K _{eq}	k (mol/m ² /s)
Solid-phase reactions		
Ca(OH) ₂ (s) + 2H ⁺ ↔ Ca ²⁺ + 2H ₂ O	22.81	7.08 × 10 ⁻⁸
C-S-H(s) + 3.6H ⁺ ↔ 1.8Ca ²⁺ + 7H ₂ O + SiO ₂ (am)	32.60	7.94 × 10 ⁻¹¹
CaCO ₃ (s) ↔ Ca ²⁺ + CO ₃ ²⁻	-8.48	4.57 × 10 ⁻⁷
SiO ₂ (am) ↔ SiO ₂ (aq)	-2.71	1.00 × 10 ⁻¹⁰
Aqueous-phase reactions		
H ₂ O ↔ H ⁺ + OH ⁻	-14.00	-
CO ₂ (aq) + H ₂ O ↔ H ⁺ + HCO ₃ ⁻	-6.35	-
HCO ₃ ⁻ ↔ H ⁺ + CO ₃ ²⁻	-10.33	-
CaCO ₃ (aq) ↔ Ca ²⁺ + CO ₃ ²⁻	-3.22	-
CaHCO ₃ ⁺ ↔ Ca ²⁺ + HCO ₃ ⁻	-1.11	-
CaOH ⁺ ↔ Ca ²⁺ + OH ⁻	-1.22	-

3. Results and Discussion

In this section, we provide the results of our numerical simulations.

3.1. Reactive Transport in Fractured Cement

Figure 2 shows the evolution of the calcite volume fraction along the fracture length at various time intervals ranging from 1 h to 72 h. As the CO₂-saturated water is introduced into the fractured cement, it accelerates the dissolution of portlandite and the release of calcium. The calcium then reacts with carbonate to form calcite. After an hour, we observe the formation of calcite in the fracture starting at 40 mm to the end of the domain. Calcite precipitation is also observed experimentally along the flow path from the middle region to the end of the core [33]. As the CO₂-saturated water continues to be injected into the system, calcite precipitation moves toward the outlet, with a starting point at 70, 80, 94, and 100 mm after 12, 24, 48, and 72 h, respectively. As the time increases, the volume fraction of calcite in the fracture also increases and reaches ~40% at the outlet after 12 h, and then it starts to decrease. This decrease can be attributed to a redissolution of calcite that prevents a complete clogging of the fracture. The supply of fresh CO₂-saturated water does not decrease during fracture sealing since our simulations are performed under constant flow rate conditions. Thus, self-sealing due to the precipitation of CaCO₃ would not lead to the complete sealing of the fracture [33]. The injection of the acidic solution into the fracture leads to portlandite dissolution and calcite precipitation. The pH in the fracture increases with calcite precipitation to more than 12 at the outlet. As the solution continues to be injected, the pH decreases over time and remains close to that of the inlet fluid between 4.0 and 5.0, with the calcite zone migrating away from the inlet. The decrease in the pH is due to the redissolution of the precipitated calcite. Similar results were obtained by Brunet et al. [12]. They obtained pH profiles that were relatively flat (between 3.4 and 4.0) and decreased over time due to the faster replenishment of the acidic water with higher flow rates. The initial fracture apertures, flow rates, and cement lengths were similar to ours.

The porosity in the fracture mirrors the calcite volume fraction trend (Figure 2b). As the calcite precipitates, the fracture porosity decreases. The rate of the calcite precipitation

equals the rate of the porosity decrease. The lowest porosity is attained toward the fracture outlet. At the inlet, the porosity remains at 100%. The decrease in fracture porosity due to calcite precipitation will lead to a decrease in fracture permeability.

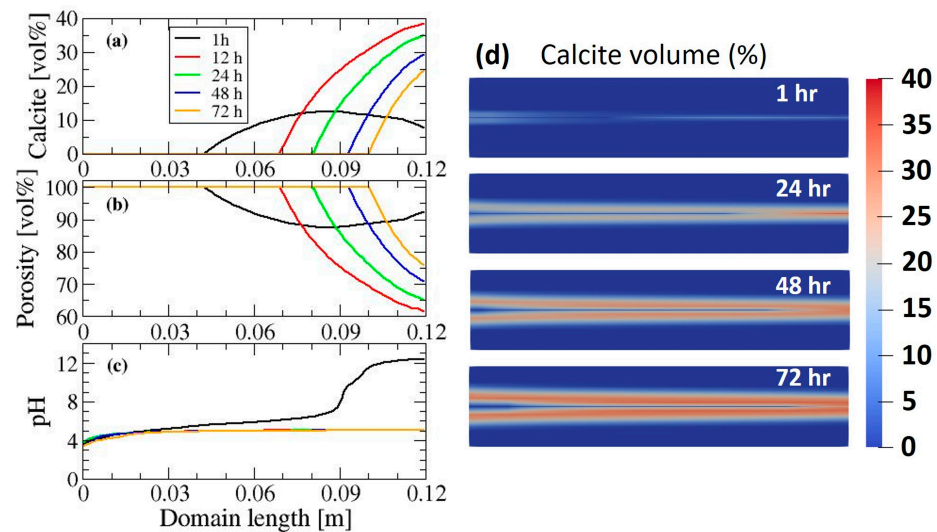


Figure 2. Predicted evolution of (a) calcite volume %, (b) porosity, and (c) pH (averaged over transverse direction) along the main flow direction within the fracture. (d) Predicted 2-D spatial profiles of calcite volume fraction evolution over time in a fractured cement.

Figure 2d shows the spatial profiles of the calcite volume fraction evolution over time in a fractured cement. It also shows the extent of the dissolution of portlandite in the system. After an hour, calcite already begins to precipitate. As the acidic solution continues to be injected at a constant rate in the system, calcite precipitation increases due to the dissolution of portlandite, especially around the fracture, resulting in the formation of an altered porous layer. In multiminerals systems with varied reactivities, it has been observed that the preferential dissolution of fast-reacting minerals often results in the development of an altered porous layer bordering the fracture, thereby affecting their dynamics and morphology [63,64]. In these figures, the average is over the transverse direction of the flow. The calcite volume % in Figure 2 is chosen for the initial width of the fracture, which is 12 μm . At the collected time, the volume % of calcite in the fracture at the inlet is zero. However, portlandite dissolution leads to calcite precipitation along the whole fracture, as shown in Figure 2d.

The introduction of the CO_2 -saturated water solution into the cement matrix leads to a decrease in the pH of the cement (Figure 3d). The initial pH of the cement is chosen to be 13 due to portlandite and other alkalis. As the acidic solution permeates through the cement matrix, portlandite is dissolved (Figure 3c). The dissolution of portlandite is accompanied by an increase in the cement porosity and a release of Ca^{2+} from the cement matrix. The diffusion of Ca^{2+} out of the cement matrix combined with the inward diffusion of the acidic solution leads to the formation of calcite in the fracture (Figure 2a). The increased porosity can lead to negative volume changes, which is not discussed in this paper. The dissolution process is more pronounced at the inlet, which is evidenced by the results in Figure 3. The cement near the inlet is directly exposed to fresh CO_2 -saturated water with the highest acidity and lowest pH values, leading to higher cement degradation rates. As time increases from 1 to 72 h, the reactive surface area decreases, the calcite volume fraction increases, the portlandite volume fraction decreases, the pH decreases, and the porosity increases. We also observe an increase in matrix permeability. This increase in permeability is due to an increase in the available pore space for the solution to diffuse into the cement matrix. This increase is more significant near the inlet front and close to the fracture.

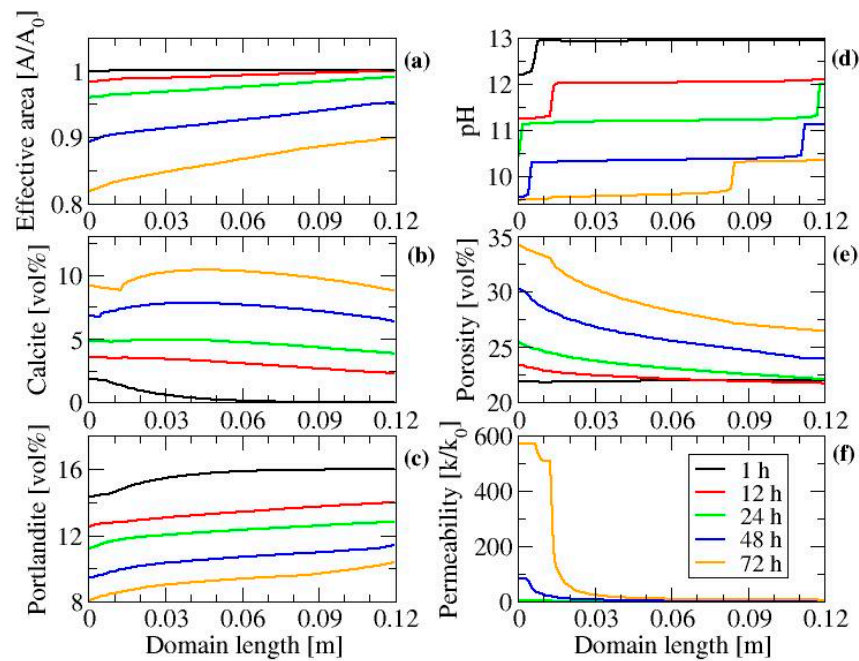


Figure 3. Evolution over time of geochemical and hydrological properties (averaged over transverse direction) of cement matrix along the flow direction. (a) Effective reactive area ratio; (b) calcite volume %; (c) portlandite volume %; (d) pH; (e) porosity; and (f) cement permeability ratio.

3.2. Effects of Cement Porosity

To investigate the effect of cement porosity on the reactive transport of CO_2 -saturated water, we vary the cement porosity, while the remaining parameters and initial conditions stay the same. In this case, the cement is represented by 13 vol % of portlandite and 72 vol % C-S-H, with an initial cement porosity of 15%, based on batch experiments [37]. The results after 48 h are collected and presented in Figures 4 and 5. We observe from our results that a change in the cement porosity has a small effect on the fracture properties. That effect is seen in the calcite precipitation and fracture porosity at the outlet (Figure 4).

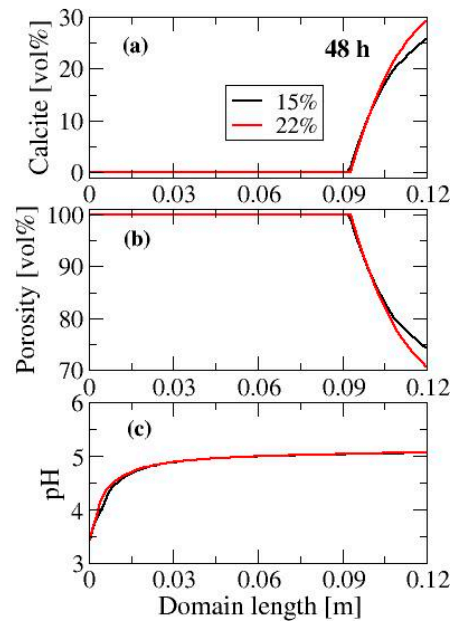


Figure 4. Effect of cement porosity on the fracture properties: Calcite (a); Porosity (b); pH (c). The data are collected after 48 h and are averaged over transverse direction. Red and black lines are for the 15 and 22% porosities, respectively.

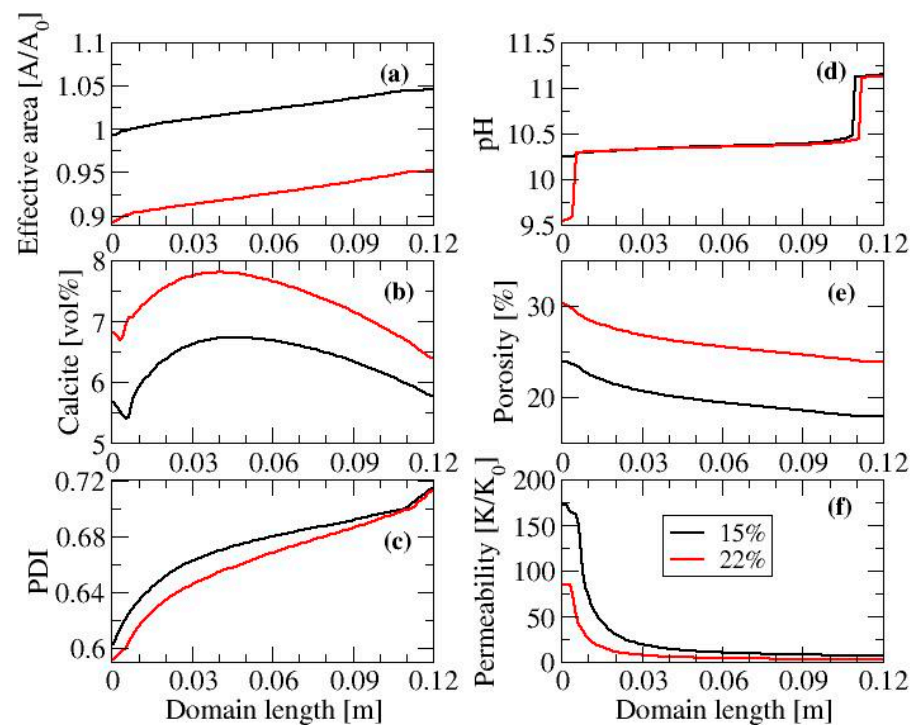


Figure 5. Effect of cement porosity on the properties of cement matrix after 48 h. Red and black lines are for the 15 and 22% porosities, respectively; Effective area (a); Calcite (b); PDI (c); pH (d); Porosity (e); Permeability (f).

The effect of the cement porosity is mostly seen in the cement matrix. A higher porosity means that there is more empty volume for the solution to flow through the matrix. The effective reactive surface area for the 22% porosity decreases rapidly compared to the 15% porosity at a ratio of ~ 1.11 . This decrease is due to the rapid dissolution of portlandite in the 22% porosity, as shown in Figure 5c, where we plotted the portlandite depletion index (PDI), which is the ratio of the total portlandite volume fraction over the initial portlandite volume fraction [12]. The lower the PDI, the higher the dissolution. Correspondingly, the calcite precipitation rate, the porosity profile, and the relative permeability profile are significantly higher in the 22% porosity than in the 15%. This increase ultimately increases the conducting capability of the flow in the cement matrix.

3.3. Effects of Initial Fracture Aperture Size

The fracture aperture size is one of the key characteristics for fracture opening or clogging. In this section, we vary the aperture size from $12\ \mu\text{m}$ to $96\ \mu\text{m}$ and compare the simulation results for three cases under similar flow conditions. For the three initial fracture aperture sizes of 12, 48, and $96\ \mu\text{m}$, the injection velocities are 5.47, 1.37, and $0.684\ \text{mm/s}$, producing a constant flow rate of $0.1\ \text{mL/min}$. Different responses of cement fracture conductivity have been observed when the initial fracture aperture sizes are different [65]. The amount of precipitation can increase depending on the fluid speed t through the fracture [66].

Figures 2 and 6 show that the calcite volume fraction in the fracture decreases as the fracture aperture size increases under similar flow conditions, resulting in an increase in porosity. The present results suggest that self-sealing decreases as the fracture aperture size increases. In smaller apertures, the fracture volume and, therefore, the total volume of the acidic solution are smaller, which induces higher concentrations of dissolution products that eventually lead to faster precipitation [9]. Our results also show that the calcite precipitation formation zone remains the same as the aperture size increases. The zone spans from approximately 40 mm to the outlet. This is because, under the same flow

rate, the velocities are lower in the larger apertures. The effect of the aperture size on the pH is negligible, as shown in Figures 2 and 6.

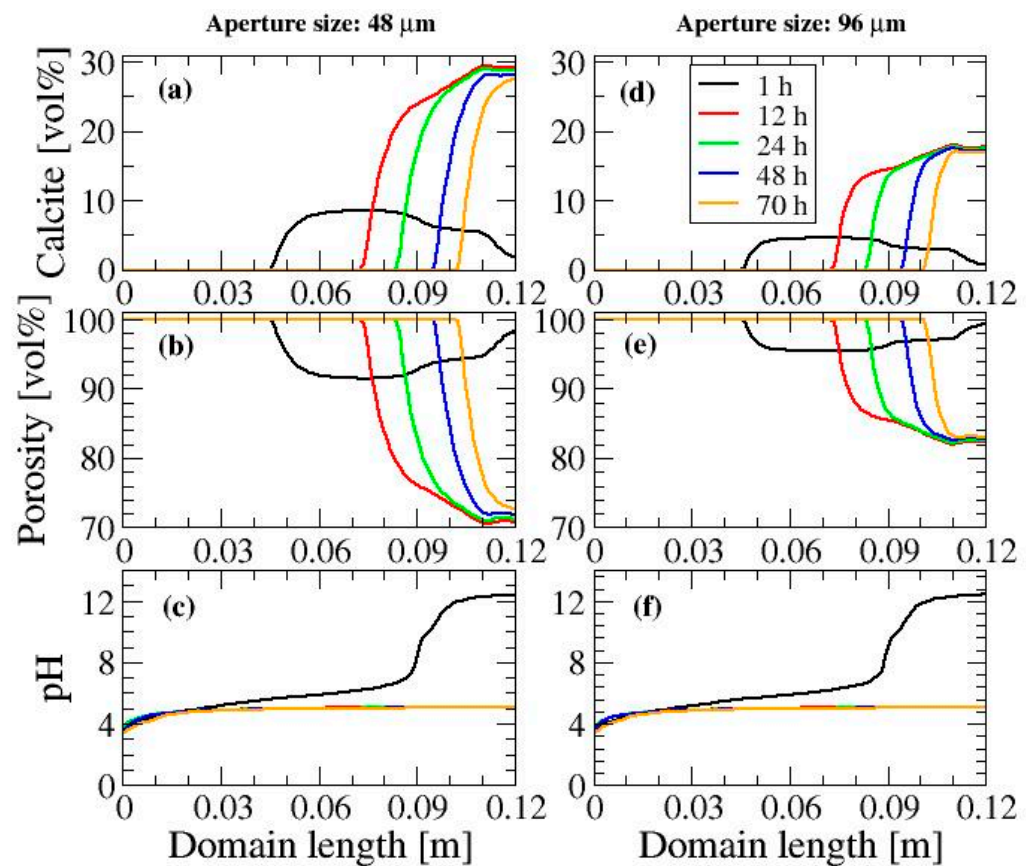


Figure 6. Effect of initial fracture aperture size on the fracture properties. Time evolution of calcite volume % (a,d), porosity (b,e), and pH (c,f) averaged over transverse direction along the main flow direction within the fractures.

The variation in the initial fracture aperture sizes has limited to no influence on the cement matrix properties during the 48 h of the continuous injection of the CO₂-saturated water solution (Figure 7). For example, the calcite volume fraction formation, the portlandite dissolution, and the pH vary in the same way, except for at the inlet front and at the outlet, where a difference is noticeable. For the smallest aperture size, 12 μm, we observe a rapid/slow dissolution of portlandite at the inlet front/outlet, resulting in a higher/lower calcite concentration at the inlet front/outlet and a decrease in the reactive surface area at the inlet front compared to the other two apertures. Consequently, the cement matrix pH for the 12 μm drops to ~9.5 at the inlet front but remains above 11 at the outlet. For the larger apertures, the pH drops but remains between 10.25 and 10.5 along the domain length. The effects of varying the aperture size on the cement porosity and the permeability averaged over the transverse direction of the main flow are minimal along the domain.

The low impact of the fracture aperture on the flow behavior in the matrix is likely due to the dominance of diffusion over advection. The Péclet number can be used to characterize the flow behavior, i.e., whether it corresponds to an advection-dominated regime or a diffusion-dominated regime. For a given characteristic length L (cement matrix width in this case), the Péclet number Pe is estimated in this work via $Pe = \frac{U_{mat}L}{D}$, where U_{mat} is the average velocity of the acidic solution in the matrix, and D is the diffusion. The estimated Pe values for the matrix of cement with fracture apertures of 12, 48, and 96 μm are 2, 0.19, and 0.05, respectively. These values suggest the dominance of a diffusive transport process in the matrix.

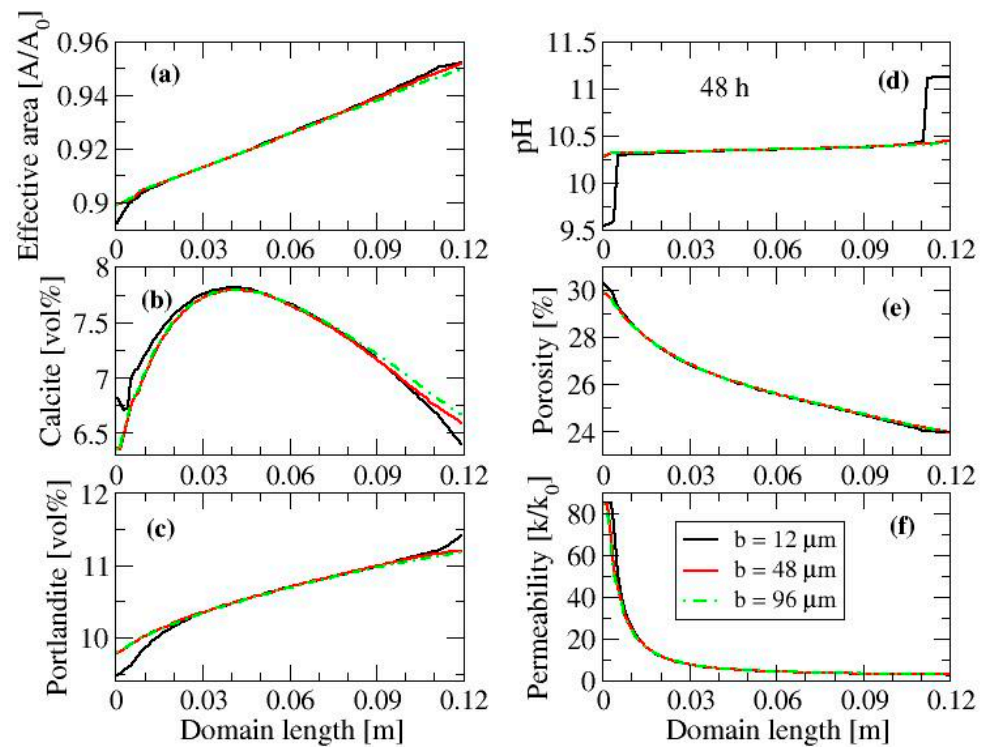


Figure 7. Effect of initial aperture size on the cement matrix properties. The data are collected after 48 h and averaged over transverse direction of the main flow. Effective area (a); Calcite (b); Portlandite (c); pH (d); Porosity (e); Permeability (f).

3.4. Effects of Fracture Surface Roughness

Lastly, we investigate the effect of the fracture shape on the flow of CO_2 -saturated water in fractured cement. The roughness of the fracture is characterized by a random zigzag shape with an average aperture of $96 \mu\text{m}$. We compare the results of the rough fracture surface (zigzag shape) with those of a smooth fracture surface with an initial average aperture size of $96 \mu\text{m}$ under similar flow conditions (Figure 8). The calcite precipitation patterns for the rough surface differ from those for the smooth surface. After 1 h, calcite precipitates up to a 10% volume fraction between 40 and 90 mm of the domain length in the rough-surface fracture in contrast to the smooth fracture, where calcite starts forming at 45 mm and extends to the outlet. As time progresses, the calcite formation in the rough fracture moves toward the outlet with a starting point at 52, 60, and 70 mm compared to at 74, 85, and 94 mm in the smooth fracture after 12, 24, and 45 h, respectively (Figure 8b,e). In the smooth fracture, the calcite distribution spans a smaller distance with a higher concentration, whereas, in the rough fracture, it spans a longer distance but with a lower concentration. The effect of the fracture shape is also reflected in the fracture porosity, which mirrors the calcite volume fraction. The lowest porosity among the two fractures is observed at the outlet of the smooth fracture and is about 82.5%. Overall, the roughness influences mineral dissolution rates by affecting the flow and the transport in the near-surface regions. It can also influence them by increasing the surface area available for reactions. Surface roughness gives rise to concentration gradients that, in general, do not develop in flat-surface geometries [15]. These local concentration gradients that result from flow and transport processes in rough-surface fractures generally limit the increase in the reaction rate.

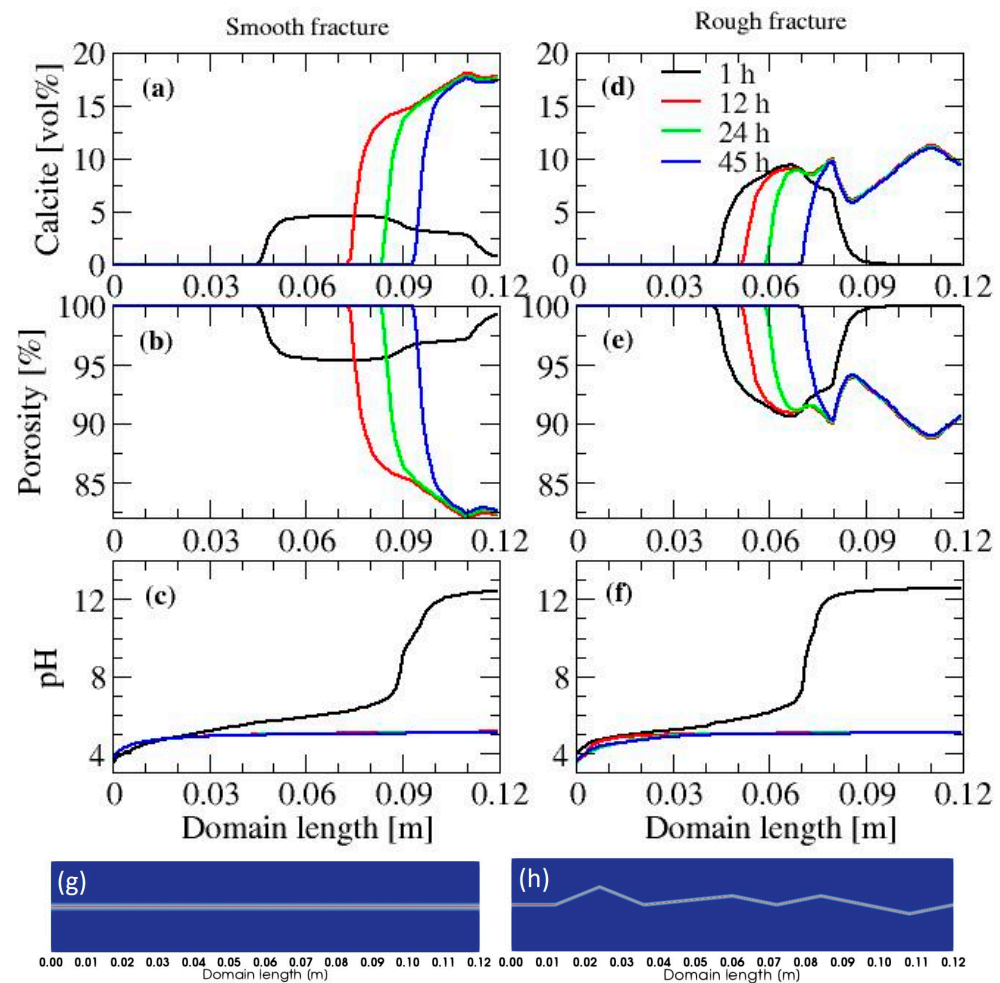


Figure 8. Effect of surface tortuosity on the fracture properties. Predicted time evolution of calcite volume % (a,d), porosity (b,e), and pH (c,f) along the domain length. Two-dimensional spatial profiles of the smooth (g) and rough or tortuous (h) cement fractures.

The effect of surface tortuosity is also observed on the pH profile after 1h of fluid injection [67]. The pH at the inlet of the smooth fracture falls to ~ 4 before increasing to ~ 7 close to 90 mm of the domain, and then it jumps to ~ 12 between 90 and 100 mm and remains constant toward the outlet. In the rough-surface fracture, the jump happens between 70 and 80 mm of the domain, and the pH remains nearly constant from 80 mm to the end of the domain. As time progresses, the pH profiles of both fractures exhibit similarities.

Figure 9 compares the horizontal U_x and the vertical U_y velocities of the flow in the smooth and the rough fractures at various times. There is a large contrast between the flows in the two fractures. In the smooth fracture, the horizontal flow velocity remains close to its maximum after 24 h. As time passes, after 45 h, U_x decreases to its minimum value close to the inlet; then, it increases as the flow moves away from the inlet and asymptotically approaches its maximum value toward the outlet. The flow in the vertical direction is almost constant and close to 0, except for at the calcite precipitation zone, where we see an increase in U_y . As for the rough fracture, the horizontal velocity after 24 h remains close to the injection velocity at 0.684 mm/s in the first 10 cm of the domain from the inlet, and then it increases sharply and reaches a maximum between 10 and 40 cm before decreasing to a value close to the injection velocity and remaining constant toward the outlet. After 45 h, U_x decreases in the first 10 cm from the inlet before increasing and reaching a maximum with a lower value than that after 24 h. Our results show that the flow in the vertical direction is very significant compared with the velocity of the same order of magnitude as U_x (Figure 9d). An increase in the velocity can indicate a transition from a

transport-controlled reaction rate to a surface reaction rate, where reaction rates depend on the surface area.

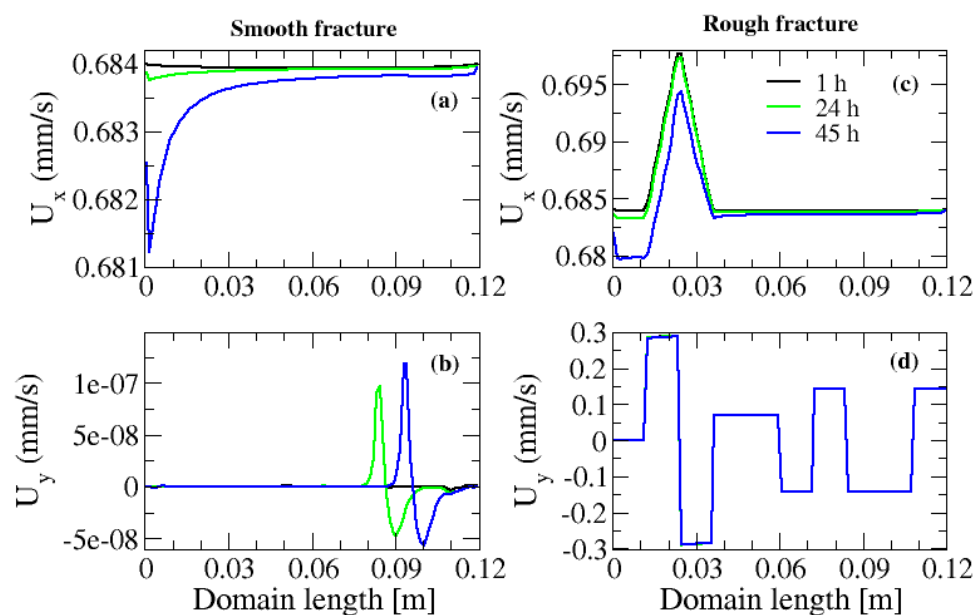


Figure 9. Horizontal U_x and vertical U_y flow velocities in the smooth (a,b) and rough or tortuous (c,d) fractures along the domain length. Negative velocities indicate the change in flow direction. The velocity is averaged over the fracture along the y direction.

4. Conclusions

In this paper, we develop a model to study the flow of a CO_2 -saturated water solution in a fractured cement. We employ a multiscale micro-continuum model based on the DBS equation, as implemented in porousMedia4Foam; this allows for the modeling of the flow and transport in fluid regions and porous regions in a single framework. The fractured domain is composed of a multimaterial system, which consists of a fast-reacting mineral, portlandite, and a slow-reacting mineral, CSH. In our simulations, flow, diffusion, and reactions are explicitly considered in the fracture and the cement matrix, allowing for an accurate depiction of mass transfer within and across domains. We investigate the impacts of cement porosity, fracture aperture size, and fracture surface roughness.

In our simulations, we use a constant flow rate of 0.1 mL/min. Our results show that smaller initial fracture apertures tend to a high mineral precipitation self-sealing. A complete sealing of the fracture is not observed. With the continuous flow of CO_2 -saturated water, portlandite at the inlet and around the fractures is consumed, and the dissolution zone propagates toward the cement matrix. The CaCO_3 initially formed could be redissolved, preventing a complete sealing of the fractures. The cement porosity has a minimal effect on fracture properties, which differs from the cement matrix. In higher-porosity cement, the reactive surface area decreases rapidly due to the rapid dissolution of the fast-reacting mineral. This decrease leads to a higher precipitation of the calcite in the altered layer.

Our simulation results show that surface roughness affects mineral dissolution and precipitation processes. For rough surfaces, calcite precipitation spans a longer distance toward the outlet in contrast to flat surfaces. Overall, fracture evolution is affected by the initial fracture geometry. In this paper, we only examine a constant injection rate, and we do not examine the effect of pressure on fracture porosity; this is an important point that is to be considered in our next study.

Author Contributions: Conceptualization, D.N.T., B.K. and M.M.; methodology, D.N.T. and M.M.; software, D.N.T.; validation, D.N.T.; formal analysis, D.N.T. and M.M.; writing—review and editing, D.N.T., B.K. and M.M. All authors have read and agreed to the published version of the manuscript.

Funding: This research received no external funding.

Data Availability Statement: Not applicable.

Disclaimer: This work was completed at the National Energy Technology Laboratory (NETL) with support from the U.S. Department of Energy’s (DOE) Office of Fossil Energy and Carbon Management. This report was prepared as an account of work sponsored by an agency of the United States Government. Neither the United States Government nor any agency thereof, nor any of their employees, makes any warranty, expressed or implied, or assumes any legal liability or responsibility for the accuracy, completeness, or usefulness of any information, apparatus, product, or process disclosed, or represents that its use would not infringe privately owned rights. Reference herein to any specific commercial product, process, or service by trade name, trademark, manufacturer, or otherwise does not necessarily constitute or imply its endorsement, recommendation, or favoring by the United States Government or any agency thereof. The views and opinions of authors expressed herein do not necessarily state or reflect those of the United States Government or any agency hereof.

Conflicts of Interest: The authors declare no conflict of interest.

References

1. Blomberg, A.E.A.; Waarum, I.-K.; Totland, C.; Eek, E. Marine monitoring for offshore geological carbon storage—A review of strategies, technologies and trends. *Geosciences* **2021**, *11*, 383. [\[CrossRef\]](#)
2. Phuoc, T.; Massoudi, M. Harvesting the potential of CO₂ before it is injected into geological reservoirs. *J. Energy Power Technol.* **2021**, *3*, 050. [\[CrossRef\]](#)
3. Phuoc, T.X.; Massoudi, M. Using CO₂ as a cooling fluid for power plants: A novel approach for CO₂ storage and utilization. *Appl. Sci.* **2021**, *11*, 4974. [\[CrossRef\]](#)
4. Khan, C.; Pearce, J.K.; Golding, S.D.; Rudolph, V.; Underschultz, J.R. Carbon storage potential of north american oil & gas produced water injection with surface dissolution. *Geosciences* **2021**, *11*, 123.
5. Le Gallo, Y.; De Dios, J.C. Geological model of a storage complex for a CO₂ storage operation in a naturally-fractured carbonate formation. *Geosciences* **2018**, *8*, 354. [\[CrossRef\]](#)
6. Phuoc, T.X.; Massoudi, M.; Wang, P.; McKoy, M.L. Heat losses associated with the upward flow of air, water, CO₂ in geothermal production wells. *Int. J. Heat Mass Transf.* **2019**, *132*, 249–258. [\[CrossRef\]](#)
7. Phuoc, T.X.; Massoudi, M.; Wang, P.; McKoy, M.L. A study of temperature distribution and thermal stresses in a hot rock due to rapid cooling. *J. Heat Transf.* **2020**, *142*, 042302. [\[CrossRef\]](#)
8. Hoteit, H.; Fahs, M.; Soltanian, M.R. Assessment of CO₂ injectivity during sequestration in depleted gas reservoirs. *Geosciences* **2019**, *9*, 199. [\[CrossRef\]](#)
9. Cao, P.; Karpyn, Z.T.; Li, L. Self-healing of cement fractures under dynamic flow of CO₂-rich brine. *Water Resour. Res.* **2015**, *51*, 4684–4701. [\[CrossRef\]](#)
10. Huerta, N.J.; Hesse, M.A.; Bryant, S.L.; Strazisar, B.R.; Lopano, C.L. Experimental evidence for self-limiting reactive flow through a fractured cement core: Implications for time-dependent wellbore leakage. *Environ. Sci. Technol.* **2013**, *47*, 269–275. [\[CrossRef\]](#)
11. Huerta, N.J.; Hesse, M.A.; Bryant, S.L.; Strazisar, B.R.; Lopano, C. Reactive transport of CO₂-saturated water in a cement fracture: Application to wellbore leakage during geologic CO₂ storage. *Int. J. Greenh. Gas Control* **2016**, *44*, 276–289. [\[CrossRef\]](#)
12. Brunet, J.-P.L.; Li, L.; Karpyn, Z.T.; Huerta, N.J. Fracture opening or self-sealing: Critical residence time as a unifying parameter for cement–CO₂–brine interactions. *Int. J. Greenh. Gas Control* **2016**, *47*, 25–37. [\[CrossRef\]](#)
13. Iyer, J.; Walsh, S.D.C.; Hao, Y.; Carroll, S.A. Assessment of two-phase flow on the chemical alteration and sealing of leakage pathways in cemented wellbores. *Int. J. Greenh. Gas Control* **2018**, *69*, 72–80. [\[CrossRef\]](#)
14. Starchenko, V.; Marra, C.J.; Ladd, A.J.C. Three-dimensional simulations of fracture dissolution. *J. Geophys. Res. Solid Earth* **2016**, *121*, 6421–6444. [\[CrossRef\]](#)
15. Deng, H.; Molins, S.; Trebotich, D.; Steefel, C.; DePaolo, D. Pore-scale numerical investigation of the impacts of surface roughness: Upscaling of reaction rates in rough fractures. *Geochim. Cosmochim. Acta* **2018**, *239*, 374–389. [\[CrossRef\]](#)
16. Deng, H.; Fitts, J.P.; Tappero, R.V.; Kim, J.J.; Peters, C.A. Acid erosion of carbonate fractures and accessibility of arsenic-bearing minerals: In operando synchrotron-based microfluidic experiment. *Environ. Sci. Technol.* **2020**, *54*, 12502–12510. [\[CrossRef\]](#)
17. Molins, S. Reactive interfaces in direct numerical simulation of pore-scale processes. *Rev. Mineral. Geochem.* **2015**, *80*, 461–481. [\[CrossRef\]](#)
18. Starchenko, V.; Ladd, A.J.C. The development of wormholes in laboratory-scale fractures: Perspectives from three-dimensional simulations. *Water Resour. Res.* **2018**, *54*, 7946–7959. [\[CrossRef\]](#)
19. Prasianakis, N.I.; Curti, E.; Kosakowski, G.; Poonosamy, J.; Churakov, S.V. Deciphering pore-level precipitation mechanisms. *Sci. Rep.* **2017**, *7*, 13765. [\[CrossRef\]](#)

20. Tartakovsky, A.M.; Trask, N.; Pan, K.; Jones, B.; Pan, W.; Williams, J.R. Smoothed particle hydrodynamics and its applications for multiphase flow and reactive transport in porous media. *Comput. Geosci.* **2016**, *20*, 807–834. [[CrossRef](#)]
21. Kang, Q.; Lichtner, P.C.; Viswanathan, H.S.; Abdel-Fattah, A.I. Pore scale modeling of reactive transport involved in geologic CO₂ sequestration. *Transp. Porous Media* **2010**, *82*, 197–213. [[CrossRef](#)]
22. Soulaire, C.; Maes, J.; Roman, S. Computational microfluidics for geosciences. *Front. Water* **2021**, *3*, 643714. [[CrossRef](#)]
23. Molins, S.; Soulaire, C.; Prasianakis, N.I.; Abbasi, A.; Poncet, P.; Ladd, A.J.; Starchenko, V.; Roman, S.; Trebotich, D.; Tchelepi, H.A. Simulation of mineral dissolution at the pore scale with evolving fluid–solid interfaces: Review of approaches and benchmark problem set. *Comput. Geosci.* **2021**, *25*, 1285–1318. [[CrossRef](#)]
24. Noirielle, C.; Soulaire, C. Pore-scale imaging and modelling of reactive flow in evolving porous media: Tracking the dynamics of the fluid–rock interface. *Transp. Porous Media* **2021**, *140*, 181–213. [[CrossRef](#)]
25. Molins, S.; Trebotich, D.; Arora, B.; Steefel, C.I.; Deng, H. Multi-scale model of reactive transport in fractured media: Diffusion limitations on rates. *Transp. Porous Media* **2019**, *128*, 701–721. [[CrossRef](#)]
26. Molins, S.; Knabner, P. Multiscale approaches in reactive transport modeling. *Rev. Mineral. Geochem.* **2019**, *85*, 27–48. [[CrossRef](#)]
27. Yousefzadeh, M.; Battiato, I. Physics-based hybrid method for multiscale transport in porous media. *J. Comput. Phys.* **2017**, *344*, 320–338. [[CrossRef](#)]
28. Steefel, C.I.; Beckingham, L.E.; Landrot, G. Micro-continuum approaches for modeling pore-scale geochemical processes. *Rev. Mineral. Geochem.* **2015**, *80*, 217–246. [[CrossRef](#)]
29. Soulaire, C.; Tchelepi, H.A. Micro-continuum approach for pore-scale simulation of subsurface processes. *Transp. Porous Media* **2016**, *113*, 431–456. [[CrossRef](#)]
30. Carrillo, F.J.; Bourg, I.C.; Soulaire, C. Multiphase flow modeling in multiscale porous media: An open-source micro-continuum approach. *J. Comput. Phys. X* **2020**, *8*, 100073. [[CrossRef](#)]
31. You, J.; Lee, K.J. A pore-scale investigation of surface roughness on the evolution of natural fractures during acid dissolution using dbS method. *J. Pet. Sci. Eng.* **2021**, *204*, 108728. [[CrossRef](#)]
32. Zhang, Q.; Deng, H.; Dong, Y.; Molins, S.; Li, X.; Steefel, C. Investigation of coupled processes in fractures and the bordering matrix via a micro-continuum reactive transport model. *Water Resour. Res.* **2022**, *58*, e2021WR030578. [[CrossRef](#)]
33. Min, Y.; Montross, S.; Spaulding, R.; Brandi, M.; Huerta, N.; Thomas, R.; Kutchko, B. Alteration of fractured foamed cement exposed to CO₂-saturated water: Implications for well integrity. *Environ. Sci. Technol.* **2021**, *55*, 13244–13253. [[CrossRef](#)] [[PubMed](#)]
34. Tafen, D.N.; Kutchko, B.; Massoudi, M. *A Brief Overview of Reactive Transport Codes Used in CO₂ Applications*; Technical Report.DOE/NETL-2022/3733; National Energy Technology Laboratory (NETL): Pittsburgh, PA, USA; Morgantown, WV, USA; Albany, OR, USA, 2022.
35. Nelson, E.B.; Guillot, D. *Well Cementing*; Schlumberger: Houston, TX, USA, 2006.
36. Taylor, H.F. *Cement Chemistry*; Thomas Telford: London, UK, 1997; Volume 2.
37. Kutchko, B.G.; Strazisar, B.R.; Dzombak, D.A.; Lowry, G.V.; Thaulow, N. Degradation of well cement by CO₂ under geologic sequestration conditions. *Environ. Sci. Technol.* **2007**, *41*, 4787. [[CrossRef](#)] [[PubMed](#)]
38. Beavers, G.S.; Joseph, D.D. Boundary conditions at a naturally permeable wall. *J. Fluid Mech.* **1967**, *30*, 197–207. [[CrossRef](#)]
39. Beckermann, C.; Viskanta, R. Natural convection solid/liquid phase change in porous media. *Int. J. Heat Mass Transf.* **1988**, *31*, 35–46. [[CrossRef](#)]
40. Bennon, W.; Incropera, F. A continuum model for momentum, heat and species transport in binary solid-liquid phase change systems—I. Model formulation. *Int. J. Heat Mass Transf.* **1987**, *30*, 2161–2170. [[CrossRef](#)]
41. Bousquet-Melou, P.; Goyeau, B.; Quintard, M.; Fichot, F.; Gobin, D. Average momentum equation for interdendritic flow in a solidifying columnar mushy zone. *Int. J. Heat Mass Transf.* **2002**, *45*, 3651–3665. [[CrossRef](#)]
42. Brinkman, H.C. A calculation of the viscosity and the sedimentation constant for solutions of large chain molecules taking into account the hampered flow of the solvent through these molecules. *Physica* **1947**, *13*, 447–448. [[CrossRef](#)]
43. Ochoa-Tapia, J.A.; Whitaker, S. Momentum transfer at the boundary between a porous medium and a homogeneous fluid—I. Theoretical development. *Int. J. Heat Mass Transf.* **1995**, *38*, 2635–2646. [[CrossRef](#)]
44. Quintard, M.; Whitaker, S. Dissolution of an immobile phase during flow in porous media. *Ind. Eng. Chem. Res.* **1999**, *38*, 833–844. [[CrossRef](#)]
45. Soulaire, C.; Pavuluri, S.; Claret, F.; Tournassat, C. PorousMedia4Foam: Multi-scale open-source platform for hydro-geochemical simulations with openfoam[®]. *Environ. Model. Softw.* **2021**, *145*, 105199. [[CrossRef](#)]
46. Soulaire, C.; Roman, S.; Kovscek, A.; Tchelepi, H.A. Mineral dissolution and wormholing from a pore-scale perspective. *J. Fluid Mech.* **2017**, *827*, 457–483. [[CrossRef](#)]
47. Lasaga, A.C. Transition state theory. In *Kinetics of Geochemical Processes*; Chapter 4; Anthonio, C.L., James, K., Eds.; De Gruyter: Berlin, Germany; Boston, MA, USA, 1981; pp. 135–170.
48. Steefel, C.I.; Lasaga, A.C. A coupled model for transport of multiple chemical species and kinetic precipitation/dissolution reactions with application to reactive flow in single phase hydrothermal systems. *Am. J. Sci.* **1994**, *294*, 529–592. [[CrossRef](#)]
49. Xie, M.; Mayer, K.U.; Claret, F.; Alt-Epping, P.; Jacques, D.; Steefel, C.; Chiaberge, C.; Simunek, J. Implementation and evaluation of permeability-porosity and tortuosity-porosity relationships linked to mineral dissolution-precipitation. *Comput. Geosci.* **2015**, *19*, 655–671. [[CrossRef](#)]

50. Poonoosamy, J.; Wanner, C.; Alt Epping, P.; Águila, J.F.; Samper, J.; Montenegro, L.; Xie, M.; Su, D.; Mayer, K.U.; Mäder, U.; et al. Benchmarking of reactive transport codes for 2d simulations with mineral dissolution–precipitation reactions and feedback on transport parameters. *Comput. Geosci.* **2021**, *25*, 1337–1358. [[CrossRef](#)]
51. Bear, J. *Dynamics of Fluids in Porous Media*; American Elsevier Publishing Company, Inc.: New York, NY, USA, 1972.
52. Issa, R.I. Solution of the implicitly discretised fluid flow equations by operator-splitting. *J. Comput. Phys.* **1986**, *62*, 40–65. [[CrossRef](#)]
53. Patankar, S.V. *Numerical Heat Transfer and fluid Flow*; Taylor & Francis: Abingdon, UK, 1980.
54. Parkhurst, D.L.; Appelo, C. Description of input and examples for phreeqc version 3—A computer program for speciation, batch-reaction, one-dimensional transport, and inverse geochemical calculations. *US Geol. Surv. Tech. Methods* **2013**, *6*, 497.
55. Parkhurst, D.L.; Wissmeier, L. Phreeqcrm: A reaction module for transport simulators based on the geochemical model phreeqc. *Adv. Water Resour.* **2015**, *83*, 176–189. [[CrossRef](#)]
56. Pavuluri, S.; Tournassat, C.; Claret, F.; Soulaïne, C. Reactive transport modeling with a coupled openfoam®-phreeqc platform. *Transp. Porous Media* **2022**, *145*, 475–504. [[CrossRef](#)]
57. Brunet, J.-P.L.; Li, L.; Karpyn, Z.T.; Kutchko, B.G.; Strazisar, B.; Bromhal, G. Dynamic evolution of cement composition and transport properties under conditions relevant to geological carbon sequestration. *Energy Fuels* **2013**, *27*, 4208–4220. [[CrossRef](#)]
58. Huerta, N.J.; Wenning, Q.C.; Hesse, M.A.; Bryant, S.L.; Lopano, C.L.; Strazisar, B.R. Development of reacted channel during flow of CO₂ rich water along a cement fracture. *Energy Procedia* **2013**, *37*, 5692–5701. [[CrossRef](#)]
59. Dávila, G.; Cama, J.; Chaparro, M.C.; Lothenbach, B.; Schmitt, D.R.; Soler, J.M. Interaction between CO₂-rich acidic water, hydrated portland cement and sedimentary rocks: Column experiments and reactive transport modeling. *Chem. Geol.* **2021**, *572*, 120122. [[CrossRef](#)]
60. Marty, N.C.M.; Tournassat, C.; Burnol, A.; Giffaut, E.; Gaucher, E.C. Influence of reaction kinetics and mesh refinement on the numerical modelling of concrete/clay interactions. *J. Hydrol.* **2009**, *364*, 58–72. [[CrossRef](#)]
61. Marty, N.C.M.; Claret, F.; Lassin, A.; Tremosa, J.; Blanc, P.; Madé, B.; Giffaut, E.; Cochepin, B.; Tournassat, C. A database of dissolution and precipitation rates for clay-rocks minerals. *Appl. Geochem.* **2015**, *55*, 108–118. [[CrossRef](#)]
62. Wolery, T.J.; Jackson, K.J.; Bourcier, W.L.; Bruton, C.J.; Viani, B.E.; Knauss, K.G.; Delany, J.M. Current status of the eq3/6 software package for geochemical modeling. In *Chemical Modeling of Aqueous Systems II*; American Chemical Society: Washington, DC, USA, 1990; Volume 416, pp. 104–116.
63. Laubach, S.E.; Lander, R.H.; Criscenti, L.J.; Anovitz, L.M.; Urai, J.L.; Pollyea, R.M.; Hooker, J.N.; Narr, W.; Evans, M.A.; Kerisit, S.N.; et al. The role of chemistry in fracture pattern development and opportunities to advance interpretations of geological materials. *Rev. Geophys.* **2019**, *57*, 1065–1111. [[CrossRef](#)]
64. Noiriël, C.; Gouze, P.; Madé, B. 3d analysis of geometry and flow changes in a limestone fracture during dissolution. *J. Hydrol.* **2013**, *486*, 211–223. [[CrossRef](#)]
65. Luquot, L.; Abdoulghafour, H.; Gouze, P. Hydro-dynamically controlled alteration of fractured portland cements flowed by CO₂-rich brine. *Int. J. Greenh. Gas Control* **2013**, *16*, 167. [[CrossRef](#)]
66. Nguyen, P.; Guthrie, G.D.; Carey, J.W. Experimental validation of self-sealing in wellbore cement fractures exposed to high-pressure, CO₂-saturated solutions. *Int. J. Greenh. Gas Control* **2020**, *100*, 103112. [[CrossRef](#)]
67. He, X.; Sinan, M.; Kwak, H.; Hoteit, H. A corrected cubic law for single-phase laminar flow through rough-walled fractures. *Adv. Water Resour.* **2021**, *154*, 103984. [[CrossRef](#)]

Disclaimer/Publisher’s Note: The statements, opinions and data contained in all publications are solely those of the individual author(s) and contributor(s) and not of MDPI and/or the editor(s). MDPI and/or the editor(s) disclaim responsibility for any injury to people or property resulting from any ideas, methods, instructions or products referred to in the content.